FULL PAPER

Rewritable Paper

ADVANCED
FUNCTIONA
MATERIALS
www.afm-journal.d

Bistable and Reconfigurable Photonic Crystals— Electroactive Shape Memory Polymer Nanocomposite for Ink-Free Rewritable Paper

Yu Xie, Yuan Meng, Wenxin Wang, Elric Zhang, Jinsong Leng, and Qibing Pei*

Paper has remained the world's most-widely accessible information medium even as sustainable and reusable paper replacements have attracted increasing attention. Here, an ink-free rewritable paper concept is developed that combines recent developments in photonic crystals, shape memory polymers, and electroactive polymers in a nanocomposite that matches the benefits of paper as a zero-energy, long-term data storage medium, but provides the additional advantage of rewritability. The rewritable paper consists of a ferroferric oxide-carbon (Fe_3O_4@C) core–shell nanoparticle (NP)-based photonic crystal embedded in a bistable electroactive polymer (BSEP). Electrical actuation induces large deformation in the z-axis of the nanocomposite, creating distinct color change in the actuated area. This nanocomposite stores high fidelity color images without inks, the images remain stable after more than a year of storage in ambient conditions, and the stored images can then be rewritten over 500 times without degrading. A seven-segment numerical display is also demonstrated.

1. Introduction

Recent attempts to create and popularize rewritable paper can greatly lessen the heavy environmental burden brought about by traditional pulp and paper industry.[1,2] Currently, paper-replacement effort is developing around several distinct technologies: electrophoretic inks,[3–7] electrowetting inks,[8,9] cholesteric liquid crystals,[10–13] reprintable coatings on paper,[14–17] and responsive photonic crystals.[18–39] Microencapsulated

electrophoretic display was first introduced by an MIT group in 1998,[3] which quickly enabled the commercially successful, monochromic e-readers popular for their low power consumption due to its bistability and paper-like legibility under illumination. A reliable full-color electrophoretic e-paper with simple fabrication process is yet to be achieved.[4,5] Current proposals either suffer from significant reflected light intensity loss due to color filters or require complex manufacturing processes to create subpixels with different colors and convoluted charging system.[6,7] Electrowetting displays are another commercialized electronic paper that was invented by Liquavista in 2003.[8] They were capable of frame rates suitable for video play with their fast switching speed through applied voltages.[9] However, electrowetting displays are not bistable, and they consume extra energy to keep the pixels in uncolored states. Kent Displays developed the most paper-like writing tablet, the Boogie board, which delivers a natural writing experience based on the reorientation of cholesteric liquid crystals (CLCs) under stylus pressure.[10–13] CLC displays also consume zero energy to maintain the written contents due to the inherent bistability of the cholesteric texture. However, the pitch of the underlying CLC, and by extension the displayed color, is predetermined during manufacturing, making the display elements monochromatic. As for reprintable paper coatings, reconfigurable dyes are adaptable to laser or ink-jet printer designs,[14–17] but the dyes are usually toxic and cost prohibitive, and the colors are only temporary, for they disappear over the course of a few days as the organic dyes oxidize.

Compared to dyes used in most current commercial e-papers, photonic crystals, which derive their colors from structures, exhibit brighter colors, are more stable, and are resistant to photobleaching.[40] Furthermore, full-color presentation is easier to achieve without needing complicated subpixel systems, as the reflected color (also called the "stopband") of the photonic crystals is easily modulated by changing the lattice constant or the refractive index of the photonic crystal, achievable through pH control, chemical vapors, humidity variation, solvent swelling, temperature changes, or electric and magnetic fields.[26,29,34,41–49] One example of ink-based rewritable photonic paper used various inks to cause differing degrees of swelling in the polymer

Y. Xie, Dr. Y. Meng, E. Zhang, Prof. Q. B. Pei
Department of Materials Science and Engineering
Henry Samueli School of Engineering and Applied Science
University of California
Los Angeles, CA 90095, USA
E-mail: qpei@seas.ucla.edu
Dr. W. X. Wang, Prof. J. S. Leng
Center for Composite Materials and Structures
Harbin Institute of Technology
Harbin 150080, P. R. China
Dr. W. X. Wang
State Key Laboratory of Marine Resource Utilization in South China Sea
Hainan University
Haikou 570228, P. R. China

The ORCID identification number(s) for the author(s) of this article can be found under https://doi.org/10.1002/adfm.201802430.

matrix, which in turn changed the lattice constant of the embedded photonic crystal to create patterns with different colors.[18–22] The photonic paper is erased by letting the ink evaporate or washing the paper in a cleansing solution. However, wet-erase procedures are usually cumbersome, and the erasing solutions degrade the rewritable paper over time, limiting their cycle lifetime. The ink itself is volatile and renders these photonic papers unsuitable for long-term information storage.[18,36] Other types of rewritable photonic paper opted to directly control the erasing step. Photonic crystals formed in a shape memory polymer (SMP) could hold stamped images, fingerprints, or other patterned images, until a heat or water evaporation-based recovery process began.[23–27] This type of photonic paper is good for handwriting, but for printing, methods reliant on stamp printing require complex fabrication processes for every new pattern. Thus, they cannot match the printing speed of traditional paper. For other methods focused on precise pattern display control, electric fields were used to manipulate the lattice constant of photonic crystals, as it is a well understood and easily implemented method. For example, electrophoresis was used to tune full-color pixels made from solvent-suspended photonic crystals.[29–32] By utilizing ionic electroactive polymers (EAPs), photonic polymer matrices can be reversibly swelled to tune colors through redox reactions or hydrogel hysteresis.[34,37–39,50] Another type of EAP, dielectric elastomers, can be employed to mechanically compress or stretch a photonic crystal polymer matrix with an applied electric field.[28,33,35] However, all electric field-based

photonic displays require additional energy input to maintain the written information. So far, no stamp-free photonic paper that is both rewritable and bistable has been developed.

In this paper, we report a facile fabrication of reconfigurable and bistable, multicolor, photonic crystals nanocomposite, combining the bistability of shape memory polymers and precise electric control from electroactive polymers. The nanocomposite displays bistable color tuning, and is rewritable without requiring inks, stamps, or a liquid-based recovery process. Colors are reflected by a ferroferric oxide-carbon ($Fe_3O_4@C$) core–shell nanoparticle (NP) based photonic crystal embedded in a bistable electroactive polymer (BSEP) matrix (**Figure 1**). Electric fields locally actuate areas of the nanocomposite film with Maxwell forces, which creates distinct color contrast ($\approx$130 nm) between the actuated and nonactuated sections due to the stopband shift. Any written pattern is maintained permanently by the thermal-responsive shape memory property until a rapid recovery process initiates. This process takes only a few seconds and simply requires exposure to heat above its phase-change temperature. A seven-segment numerical display was also demonstrated to show the ability of displaying user-defined patterns with pixelated electrodes, eliminating the need for stamps that are required in SMP-based displays. Despite significant advances in photonic crystal films from prior research into SMPs and EAPs, this paper is the first to leverage the advantages of each polymer to offset the other's deficiencies in a manner that fully satisfies the demands of a rewritable paper.
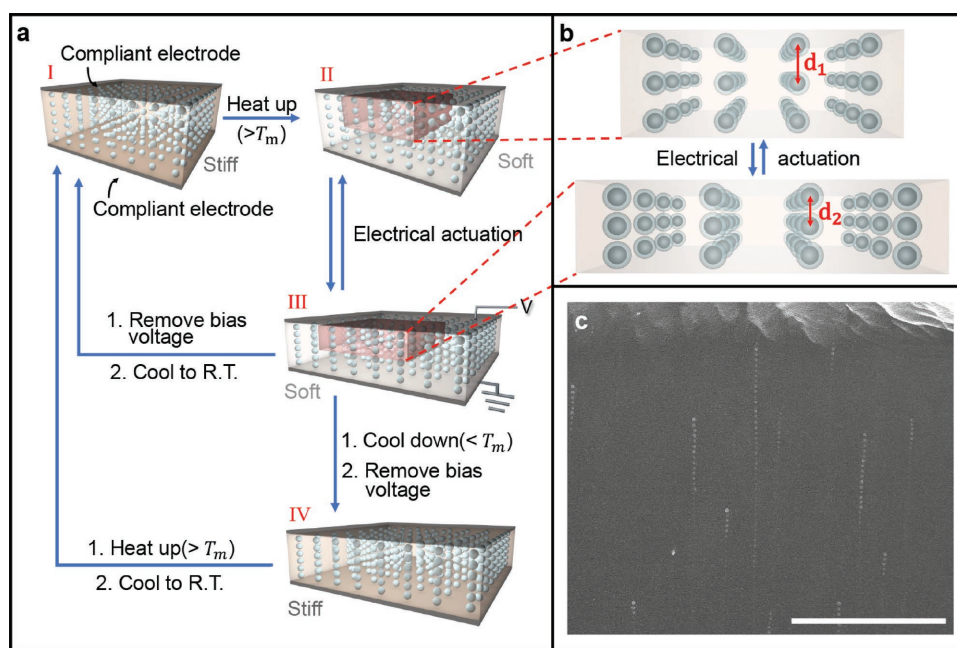

Figure 1. Schematics demonstrating the electroactive and the shape memory properties of a $Fe_3O_4@C$-BSEP photonic nanocomposite and its writing/erasing mechanism. a) The rigid nanocomposite (I) softens upon heating above its phase-changing temperature (II), applied electric field actuates the softened polymer (III), film returns to rigid state when cooled below the phase-change temperature, locking the large applied strain (IV), and the film recovers its original rigid shape (I) by heating above the phase-changing temperature and then cooling back down. b) Enlarged cross sections of the photonic nanocomposite showing the interparticle distance changing during electric field actuation. c) Cross-sectional SEM image of nanochain structures of $Fe_3O_4@C$ nanoparticles in a cured BSEP substrate. The scale bar is 5 µm in length.

**ADVANCED
SCIENCE NEWS**
www.advancedsciencenews.com

**ADVANCED
FUNCTIONAL
MATERIALS**
www.afm-journal.de

2. Preparation of Fe_3O_4@C Core-Shell Nanoparticle BSEP Nanocomposite

We chose Fe_3O_4@C core–shell nanoparticles synthesized via ferrocene hydrolysis as the building blocks of the photonic crystals. Compared with other common nanoparticles bases, such as self-assembled polystyrene or silica, Fe_3O_4@C offers both order of magnitude faster assembly time due to its superparamagnetic nature, and better color contrast because of its darker inherent color and large refractive index.[51] Furthermore, the carbon shell helps stabilize the nanoparticles and prevent them from aggregating. By manipulating the size of Fe_3O_4@C nanoparticles and the interparticle distances, we customized the reflected color of the Fe_3O_4@C-BSEP nanocomposite into visible light range. Figure S1 (Supporting Information) shows the TEM images of Fe_3O_4@C core–shell nanoparticles with different diameters. Out of the 100 to 180 nm diameter range for the Fe_3O_4@C core–shell nanoparticles that will create stopbands in the visible light range, the optimal diameters lie within 110 to 140 nm. Below 110 nm, the nanoparticles only form ordered structures under powerful magnetic fields, and they preferentially reflect blue light. Above 160 nm, the large size limits the approach of the nanoparticles as they come into contact, constricting their reflected color to red.[52]

The BSEP that forms the polymer matrix is a photocured copolymer that consists of stearyl acrylate (SA) and urethane diacrylate (UDA) in weight ratios of 40:60 to 80:20. The phase-change temperature (T_m) of the BSEP varies from 30 °C to 45 °C depending on the composition. The electroactive, shape memory properties and crystallinity of SA-UDA copolymers have been described elsewhere.[53] For demonstration purposes, we used a SA-UDA copolymer with a 60:40 weight ratio (BS60) throughout this work for its high stretchability and good fixing ratio. Figure S3 (Supporting Information) provides the structures of each components within BSEP and a schematic network structure of cured BSEP.

To create the nanocomposite, SA and UDA comonomers were first mixed with a crosslinker and a photoinitiator. Then, prepared Fe_3O_4@C powder was homogenously mixed in to create a thick slurry photonic precursor. A film of photonic slurry is then exposed to a magnetic field, which aligns the superparamagnetic Fe_3O_4@C nanoparticles into nanochain structures. The magnetic field induces a dipolar magnetic attractive force to counter the electrostatic repulsive force between the nanoparticles. A stronger magnetic field induces a stronger interparticle attractive force, decreasing the lattice constant and blue shifting the reflected spectrum. Figure S2 (Supporting Information) confirms the magnetization of Fe_3O_4@C nanoparticles at room temperature under external magnetic field. The photonic slurry is then UV cured while under a persistent external magnetic field (≈2300 G). While the photonic film exhibited a brilliant purple color before curing, it red-shifted during the curing process. After curing, the photonic crystal chains were immobilized within the polymer matrix, fixing the nanoparticle alignment, interparticle distance, and stopband. After fixation, external magnetic fields no longer significantly alter the reflection color, so the final reflected color after cure is determined by the size and concentration of Fe_3O_4@C nanoparticles. An SEM image of Fe_3O_4@C nanochain structures in cured BSEP substrate is shown in Figure 1c.

3. Nanoparticle Concentration Effect on Film Initial Color

To accommodate for the blueshift in reflectance during the actuation of the photonic nanocomposite, we experimented with different concentrations of Fe_3O_4@C nanoparticles in the precursor to achieve the optimal initial reflected color that lies on the lower energy end of the visible light range. We started with Fe_3O_4@C-monomer precursor slurries with nanoparticle concentrations of 3 to 7 wt%, which all appeared purple when exposed to a magnetic field of ≈2300 G. Though most of the samples redshifted to some degree during curing, those with higher concentrations redshifted further after curing, as shown in **Figure 2**a.

The lattice constant increase may have resulted from the stronger repulsive forces between nanochains, given that the higher NP concentration puts them in greater proximity. Specifically, applying a magnetic field before UV-cure induces a dipole–dipole interaction between individual nanoparticles. For any two nanoparticles, the force generated between them is described by Equation (1)

$$F = 3\mu^2(1 - 3\cos 2\theta)/d^4 \tag{1}$$

where μ is the effective magnetic moment of a given nanoparticle, θ is the angle between the magnetic field vector and the line intersecting the centers of both nanoparticles, and d is the interparticle distance. While $\theta < 54.09°$, the force between two nanoparticles is attractive. Whereas when $54.09° < \theta < 90°$, the force is negative.[54] When dispersed in monomers, the nanoparticles chains are balanced between the repulsive force from surface charges and the attractive force induced by magnetic field. As the curing process shrinks the film laterally, the nanochains are brought closer together. For a low nanoparticle concentration film, the nanochains are still far away to influence each other. But with a higher nanoparticle concentration, a closer interchain distance will result in an extra dipole–dipole repulsive interaction between adjacent chains. Since there is no space for nanochains to move in xy-directions, they will push away nanoparticles from adjacent chains along z direction, and thus lead to an increase in the lattice constant and red shift in the color.

The SEM images (Figure 2b) confirm the increment in NP–NP separation along the magnetic field within each nanochain (i.e., the increase in lattice constant), and the reflective spectra (Figure 2c) demonstrates the stopband red shift as nanoparticle concentration exceeds 4 wt%. The same pattern occurs for Fe_3O_4@C nanoparticles embedded in a different polymer system (PEGDA), as shown in Figure S4 (Supporting Information), which suggests that this phenomenon is not a special interaction or chance.

Table S1 (Supporting Information) contains the NP–NP distances as measured from the SEM images for each sample concentration. The calculated stopbands of these Fe_3O_4@C-BSEP nanocomposites films were derived from Bragg's diffraction equation Equation (2)

$$\lambda = 2 n_{eff} D \sin\alpha \tag{2}$$

where λ is the peak wavelength of the stopband, D represents the measured lattice constant of the photonic crystal, and n_{eff}

**ADVANCED
SCIENCE NEWS**
www.advancedsciencenews.com

**ADVANCED
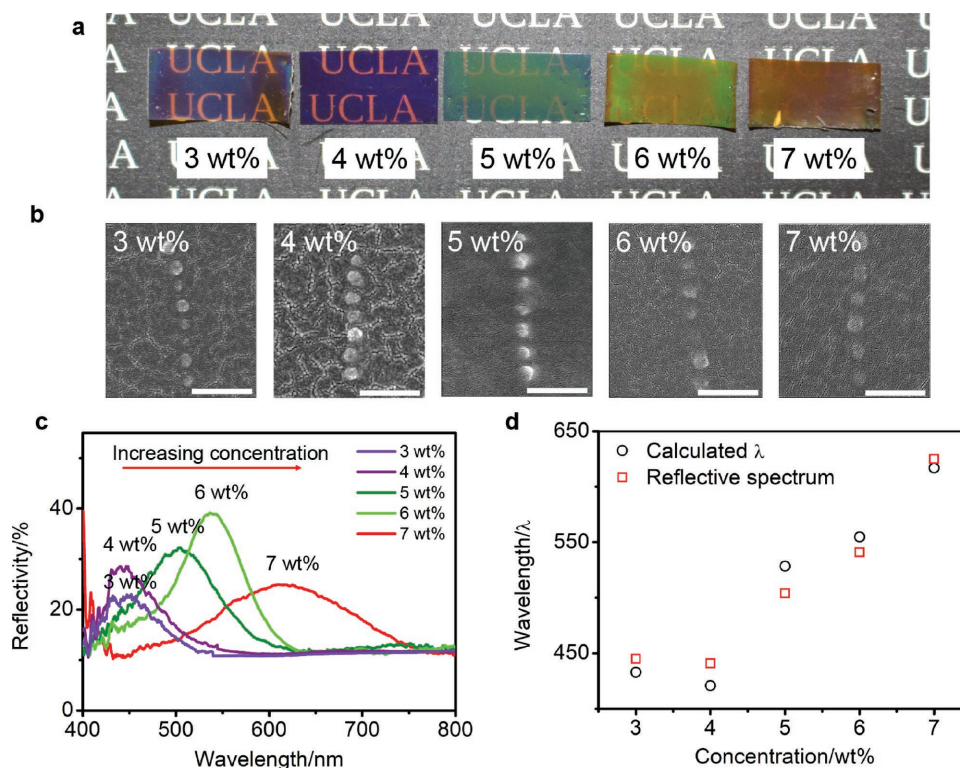FUNCTIONAL
MATERIALS**
www.afm-journal.de

Figure 2. BSEP-Fe$_3$O$_4$@C photonic nanocomposite films with increasing nanoparticle concentrations. a) Optical images of the photonic nano-composites showing red shift in base reflected color. b) Cross-sectional SEM images of the Fe$_3$O$_4$@C nanochains in the BSEP matrix. Interparticle distance increased with increasing Fe$_3$O$_4$@C weight fraction. All the scale bars are 500 nm in length. c) Reflective spectra at each concentration. d) Peak wavelength of the stopbands as a function of the concentration of nanoparticles. Black circles are calculated values based on Bragg's diffraction equation using the NP–NP distances meansured by SEM. Calculation details can be found in Supporting Information. Red square values were directly meansured by the reflective photospectrometer.

is volume-weighted average refractive index for the whole film. The Fe$_3$O$_4$@C nanoparticles used in this series of Fe$_3$O$_4$@C-BSEP nanocomposites had a core diameter of 82 nm and a C shell thickness of 44 nm measured from TEM images. The calculation of n_{eff} for each Fe$_3$O$_4$@C-BSEP nanocomposite can be found in the Supporting Information. As shown in Figure 2d, the calculated stopbands (black circles) of this series of films match well with the experimental data measured directly from the reflective spectra (red squares). More calculation details can be found in the Supporting Information.

Ultimately, based on the reflective spectra results, nanoparticle concentrations between 5 and 7 wt% produced the best finalized films with the desired initial red-green range of color.

4. Mechanical Properties Characterization

Based on previous research, we expected the BSEP to fit the desired mechanical property profile for a photonic paper, but we needed to verify its properties and understand what changes result from adding in the NPs.[53] For this purpose, we compared BSEP with 0 wt% NPs and BSEP with 7 wt% NPs, the highest NP density used in our paper. The evaluation of our thermally activated BSEP is divided into three major categories: properties of the low temperature state, properties of the high temperature state, and properties of the transition.

In the low temperature state, the BSEP must be rigid enough to store information in the form of deformation until reactivated by heat. At low temperatures, both 0 and 7 wt% have elastic moduli on the order of 10^2 MPa, more than rigid enough to endure external stimuli (**Figure 3**a). In the high temperature state, the BSEP needs a low young's modulus to lower the force requirements needed for electric field actuation. Both samples had a rubbery modulus on the order of 10^{-1} MPa; the 7 wt% rubbery modulus was slightly lower likely due to the reduced crosslinking density. The increase in mechanical loss factor (Figure 3b) for 7 wt% Fe$_3$O$_4$@C-BSEP nanocomposite compared to pure BSEP after phase transition further supports a lower crosslinking density. The increase in viscoelasticity is best explained by the weakened resilience force due to the reduced number of crosslinked bonds between the long UDA chains and dispersed nanoparticles blocking film recovery. This agrees with previously reported studies where composite networks with higher nanoparticle concentrations had lower crosslinking densities, as evidenced by a higher degree of swelling in solvent.[55]

Furthermore, the film needs high elasticity above the transition temperature so that localized deformation does not cause fracture at the border between actuated and nonactuated sections. The 7 wt% sample experienced a significantly lower fracture elongation rate at 125% compared to 286% for pure BSEP, potentially from nanoparticles impeding the extension of the
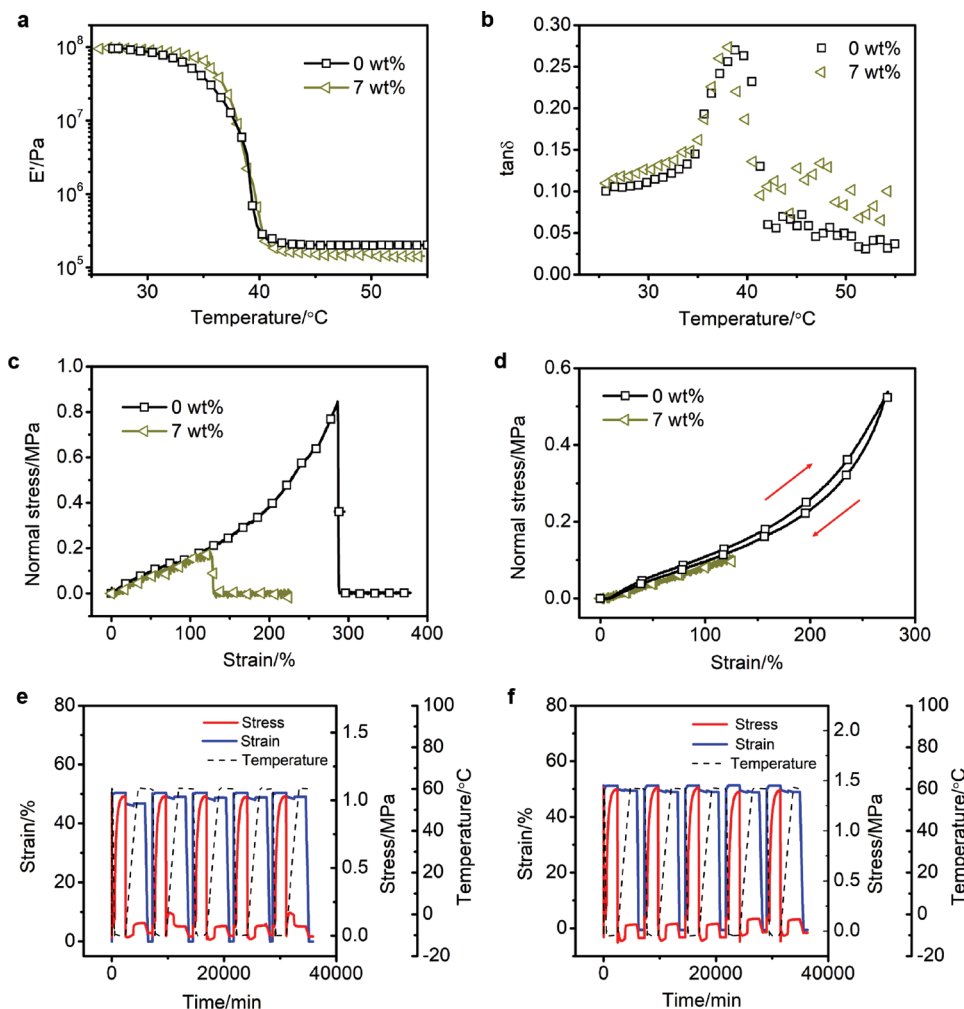
**ADVANCED
SCIENCE NEWS**
www.advancedsciencenews.com

**ADVANCED
FUNCTIONAL
MATERIALS**
www.afm-journal.de

Figure 3. Mechanical properties of a 7 wt% BSEP-Fe$_3$O$_4$@C photonic nanocomposite compared to pure BSEP. a) Storage modulus (E') as a function of temperature showing a glass transition temperature of ≈38 °C for both 7 wt% nanocomposite and pure BSEP. b) Loss factor of both 7 wt% nanocomposite and pure BSEP as a function of temperature. c) Tensile stress–strain curves. Frature strain is 125% for the 7 wt% nanocomposite and 286% for the pure BSEP. d) A tensile loading–unloading cycle for the pure BSEP polymer and 7 wt% nanocomposites. e) Shape memory cycle test for pure BSEP polymer. f) Shape memory cycle test for 7 wt% nanocomposite.

long, entangled, UDA chains (Figure 3c). Furthermore, the nonuniform nanochain distribution amplifies their inherent stress concentration behavior, which contributes to the decrease in elongation at break as well. However, 50% strain is sufficient to achieve a distinct stopband shift, which leaves a large margin before failure.

The transition region must also conform to the intended use. The transition temperature must be low enough for a conventional or household appliance to achieve quickly and inexpensively while high enough that ambient temperatures won't erase it. The transition temperature measured from the dynamic mechanical analyzer (DMA) was 38 °C, as tested with a 2 °C min^{-1} ramp rate (Figure 3a). The temperature is well within the range reasonably achievable with cheap localized heating. In addition, Figure 3d shows a cyclic tensile loading–unloading test for the pure SA-UDA polymer and 7 wt% Fe$_3$O$_4$@C-BSEP nanocomposite. Both polymers show great elastic properties dictated by tiny hysteresis loops, which helps reduce recovery time and energy loss compared to viscoelastic materials.

For shape memory properties, the fixing ratio and recovery ratio of both pure SA-UDA polymer and 7 wt% Fe$_3$O$_4$@C-BSEP nanocomposite were tested through DMA as shown in Figure 3e,f. Based on the averaged data of five cycles, the fixing ratio and recovery ratio of pure SA-UDA polymer are 96.1% and 100%; whereas the fixing ratio and recovery ratio of 7 wt% Fe$_3$O$_4$@C-BSEP nanocomposite are 96.6% and 100%, showing no obvious influence of nanoparticles to the mechanical properties of the polymer matrix.

5. Shape Memory Property Characterization and Color Change

Color contrast and color persistence are the two key parameters for evaluating Fe$_3$O$_4$@C-BSEP nanocomposite color tuning properties. Change in reflected spectra is a function of deformation of the lattice matrix, so we opted to characterize the stopband shift with a tensile load test. A sample film with
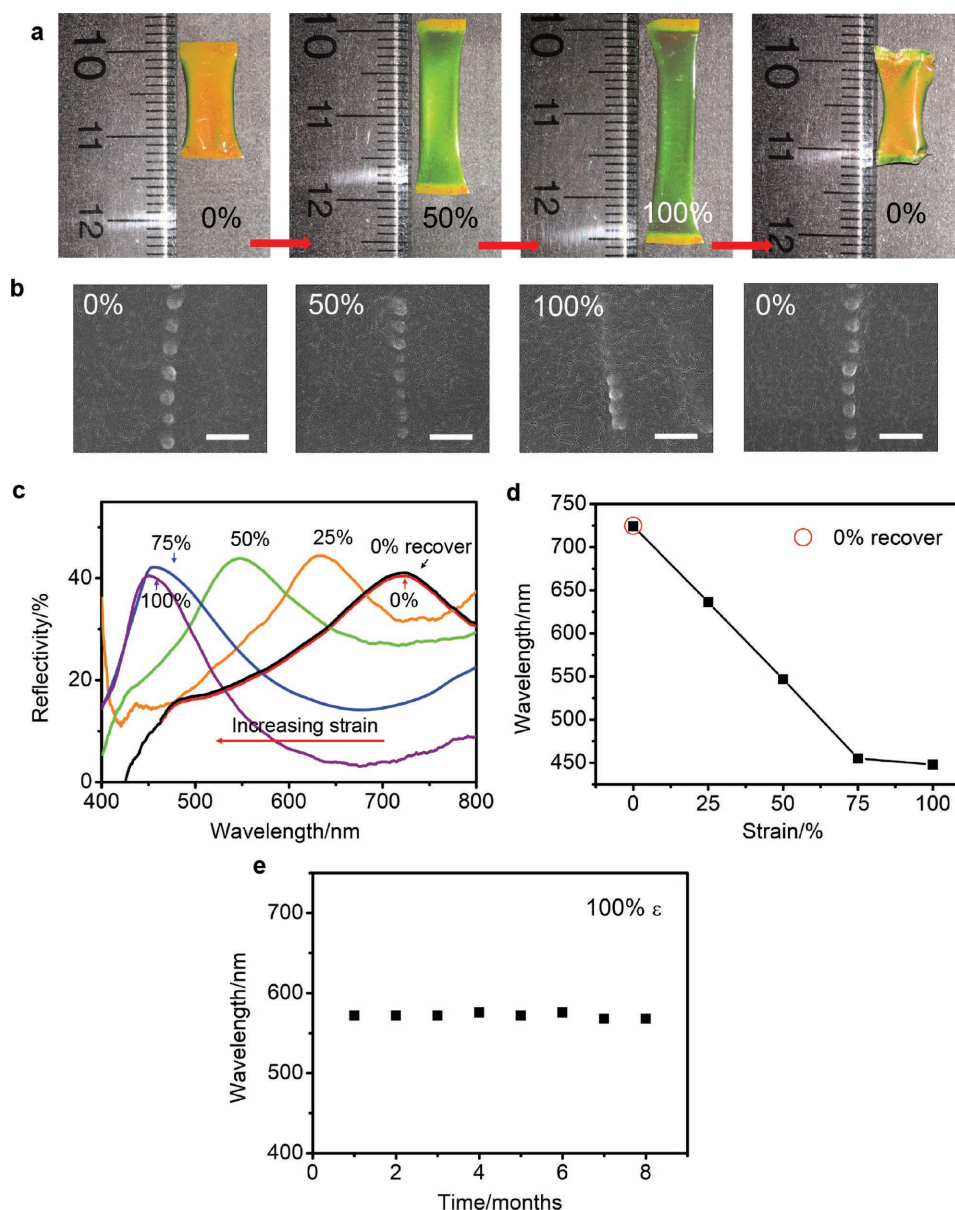
**ADVANCED
SCIENCE NEWS**
www.advancedsciencenews.com

**ADVANCED
FUNCTIONAL
MATERIALS**
www.afm-journal.de

Figure 4. Shape memory property of the photonic nanocomposite containing 6 wt% Fe_3O_4@C nanoparticles. a) Optical images of the a red photonic nanocomposite at 0%, 50%, and 100% tensile strains. Note that all of the films are freestanding and rigid at room temperature. The rightmost image is the recovered shape of the the nanocomposite film after 100% strain. b) Cross-sectional SEM images of the same photonic nanocomposite at 0%, 50%, and 100% tensile strains. Interparticle distance decreases with increasing film strain. All the scale bars are 500 nm in length. c) Reflective spectra and d) peak reflective wavelengths of this photonic nanocomposite as a function of tensile strain. "0% recover" data points in both figures indicate the complete recovery of the photonic film after 100% strain. e) Peak reflective wavelengths of a 100% strained photonic nanocomposite measured over an eight-month span.

a 10 mm × 6 mm active area was kept at 50 °C, well above the transition temperature to soft state, and stretched along a single axis (x-axis) to a maximum 100% strain with nanoparticle chains embedded along the z-axis. Strain along the x-axis induces compression along the z-axis, reducing the interparticle distance within the nanochains. The film was then cooled in the air with load to maintain the deformation and color change. Measurements of the reflected spectra and interparticle distances were taken at 25% strain intervals from 0% strain to 100% strain. 50% strain along the x-axis lead to a color change

from red to green as seen in **Figure 4**a, corresponding to a 177 nm stopband shift (Figure 4c). After stretching the sample to 75% strain, the color changed into a dark green, and further strain induced only slight darkening in the sample. At 100% strain, the stopband shifted a maximum 276 nm.

SEM images in Figure 4b and Figure S5 (Supporting Information) show the change in interparticle distance of the Fe_3O_4@C-BSEP film at different tensile strain (ε) states. Data measurements for the interparticle distances (D) and their corresponding strains (ε_z) are shown in Table S2 (Supporting

**ADVANCED
SCIENCE NEWS**

www.advancedsciencenews.com

**ADVANCED
FUNCTIONAL
MATERIALS**

www.afm-journal.de

Information). We measured 281.9 nm as the initial Fe_3O_4@C interparticle distance at 0% tensile strain based on the SEM images. Using this initial distance as the baseline and assuming a Poisson ratio of 0.5 which is typically observed for rubbery elastomers, we calculated the theoretical interparticle distances as a function of tensile strain. As shown in Table S2 (Supporting Information), the theoretical values match well with the measured distances until 75% tensile strain. At 100% tensile strain, the theoretical distance is smaller than the measured distance. In the nanocomposite, the minimum interparticle distance is constrained by the rigid nanoparticles contacting each other. The measured reflective wavelengths (λ) confirm the physical limit on compression, as there is a negligible change in wavelength between 75% and 100% strain (Figure 4c, Table S2, Supporting Information). The calculated reflective wavelengths derived from Bragg's diffraction equation and the measured Fe_3O_4@C interparticle distances are consistent with the measured reflectance data at each strain level. The large stop-band shift creates a distinct color contrast between the stretched and unstretched film, which is easily noticeable to human eyes.

In addition to pattern clarity, pattern persistence is also a critical parameter for practical applications of this nanocomposite. We tested pattern permanence by exposing a 100% strained photonic film to ambient temperature and measuring its reflectance every week. The peak reflectance wavelength data in Figure 4e shows that the 100% strained film retains its color without noticeable variation for over a year (figure represents an 8-month segment). By raising the temperature above T_m and releasing the stress on the sample, it recovers to its original state, which is also verified by the near identical reflective spectra in Figure 4c,d.

6. Electroactive Properties Characterization

The Fe_3O_4@C-BSEP photonic nanocomposite has both electroactive and shape memory properties due to the nature of the SA-UDA copolymer. Figure 1a demonstrates the working principle of this Fe_3O_4@C-BSEP nanocomposite film with compliant electrodes on each face. The rigid photonic film softens after it is heated above its T_m, at which point the photonic film is responsive to external electric fields. Under an electric field, charges along the same electrode surface repel each other, but they attract the charges from the opposite electrode surfaces, causing the film to expand in-plane but shrink in the z direction. Thus, the interparticle distance shortens, as shown in Figure 1b. This dimensional change blue-shifts the stopband, which in turn changes the color the photonic paper reflects. To prevent buckling as the nanocomposite film actuates, the film is biaxially prestretched by 15% strain in each direction using a custom 2D frame before applying the electric field.[56] As the film cooled below T_m under a maintained electric field, the deformation and blueshifted color became permanent. Below T_m, the photonic paper no longer requires the electric field to display color. Heating the film above T_m recovers its original shape and coloration.

An important step in building the electroactive photonic nanocomposite is ensuring that the electrodes that induce actuation can survive the stresses applied by the polymer as

it expands and contracts. For this purpose, we chose transparent silver nanowire (AgNW) electrodes for their visible light transparency and mechanical compliancy. We fabricated Fe_3O_4@C-BSEP composite pixel samples with patterned AgNW electrodes along the top and bottom surfaces of the film, as explained in Figure S6 (Supporting Information). Details for the electrode fabrication can be found in the Experimental Section. Each sample had a 5 mm × 5 mm "active area" covered by the electrodes and an initial sheet resistance of 15 Ω sq^{-1}. The composite electrode can be stretched to 100% linear strain and 45% area strain while keeping the transient resistance smaller than 4 kΩ. Given the high voltage, low current actuation mechanism of our BSEP, the composite film would still function with transient resistance at several MΩ. For our sample, we achieved maximum color tuning with at most 40% area strain (including prestrain), and the sheet resistance still remained below 3 kΩ (Figures S7 and S8, Supporting Information).

Now that we had an electrode capable of surviving the stresses exerted by the substrate, we tested the electroactive property of the Fe_3O_4@C-BSEP nanocomposite with a smaller inset 5 mm × 5 mm electrode area acting as a single photonic pixel with a red initial color. We began by varying the strength of the electric field from 16.7 to 26.7 kV m^{-1} in 1.1 kV m^{-1} increments with an additional baseline measurement without any electric field, shown in **Figure 5**a. Comparing the stopband against the electric field, Figure 5b reveals an inverse linear relationship, which matches well with theoretical values for the stopband, shown by red circles, that were derived from the measured strains. Details for the calculation can be found in Table S3 (Supporting Information).

Figure 5c demonstrates the writing and erasing processes of the single photonic pixel. After applying an electric field of 22.5 kV m^{-1}, the photonic pixel expanded in-plane, generating a 108 nm stopband shift from 624 to 516 nm. The heated film reverted from green to red once the electric field was switched off. Figure 5e is a visual comparison between the on and off states of the photonic pixel. The square gray area on the film is the partial discoloration by the upper AgNW electrode, as the film is otherwise uniformly red. Since the applied electric field is localized, only the middle square area of the film expanded. There was a clear color change from red to green with significant color contrast between the red background and the green written pixel as shown in video MV1 (Supporting Information). Both the activation and recovery times of the pixel measured around 0.8 s. Figure 5f is a similar photonic pixel but with a green initial color due to a different Fe_3O_4@C nanoparticle size and concentration. After electrical actuation, the area of the film between the patterned AgNWs electrodes switched from green to purple, generating a similarly distinct color change between the two states, as shown in video MV2 (Supporting Information).

The Fe_3O_4@C-BSEP nanocomposite was tested for durability by cycling it under an electric field following a square wave signal operating between 0 and 22.5 kV m^{-1}. Reflective wavelength was measured 3 s after each change in electric field to leave time for the film to equilibrate. Across 500 periods, cycling produced no appreciable change in color fidelity or film integrity, as shown in Figure 5d.
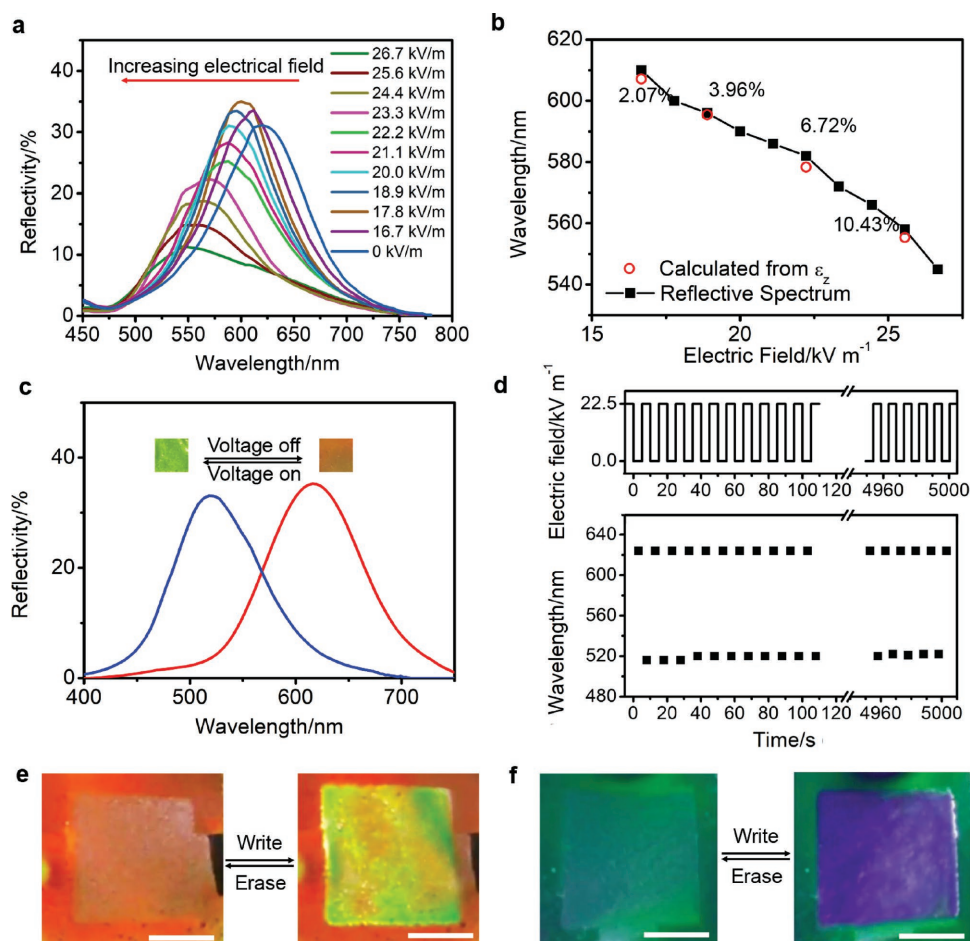
Figure 5. Electrical actuation of the photonic nanocomposite pixel above transition temperature. a) Reflective spectra with incremental increase in applied electric field. b) Peak reflective wavelengths as a function of electric field. Red open circles are stopbands calculated from thickness strains of the film, which are shown next to the circles. Calculation procedure can be found in Table S3 (Supporting Information). c) Reversible writing and erasing of a red photonic nanocomposite pixel by switching the 22.5 kV m^{-1} electrical field on and off. d) Peak reflective wavelength across 500 writing and erasing cycles following a square wave signal operating between 0 and 22.5 kV m^{-1}. e,f) Written and erased states of photonic nanocomposite pixels switching between e) red and green colors, and f) green and purple colors under electric field actuation. The color-changing area is the "active area" where the AgNW electrodes on top and bottom surfaces overlap. The scale bars are 3 mm in length.

7. Bistable Electroactive Photonic Paper

With patterned electrodes, we built a basic rewritable photonic paper demonstrating the strengths of Fe$_3$O$_4$@C-BSEP nanocomposite in color contrast and ease of operation. For conventional paper, the exhibited information cannot be changed once printed. And for SMP-based photonic paper, cumbersome fabrication of new stamps is needed to demonstrate different patterns. But for our rewritable paper, with pixelated electrode matrix, any desired patterns can be displayed by selectively actuating electrode pixels. And this photonic film can be refreshed with new patterns by selecting different electrode pixels to actuate. As a demonstration, we fabricated a 7-segmented numerical display. Details about the electrode preparation and photonic paper fabrication can be found in the Experimental section. After curing and heating it above its transition temperature, the photonic paper was green in the absence of an applied electric field. By applying a 30 kV m^{-1} electric field to specific segments of the electrode, it displayed the digits 0 to 9 in purple color against the green

background, as seen in **Figure 6**a and video MV3 (Supporting Information). The photonic paper maintained the digits without the aid of the electric field once brought below T_m, and bringing the film above the T_m erased it completely. When placed in contact with a 65 °C hot plate, the photonic paper fully recovered within a second. Recovery at more practical temperatures, e.g. 40 °C, remains below 8 s. Video MV4 (Supporting Information) shows the full recovery of a photonic paper after transferred from ambient environment (21 °C) to a 100 °C hotplate. However, the prestretch frame prevented direct contact with the hotplate, leading to a longer recovery time.

Another key parameter for the practical application of this new photonic paper is achieving a comparable resolution to conventional paper. A "UCLA" pattern in Calibri font size 10 was used as a sample to evaluate resolution limits of the photonic film. To prepare the film, a "UCLA"-shaped electrode with a feature size of 300 μm was transferred onto the back side of a photonic paper. Once actuated by an electric field, the "UCLA" pattern showed up clearly, as demonstrated in Figure 6b. The size of the
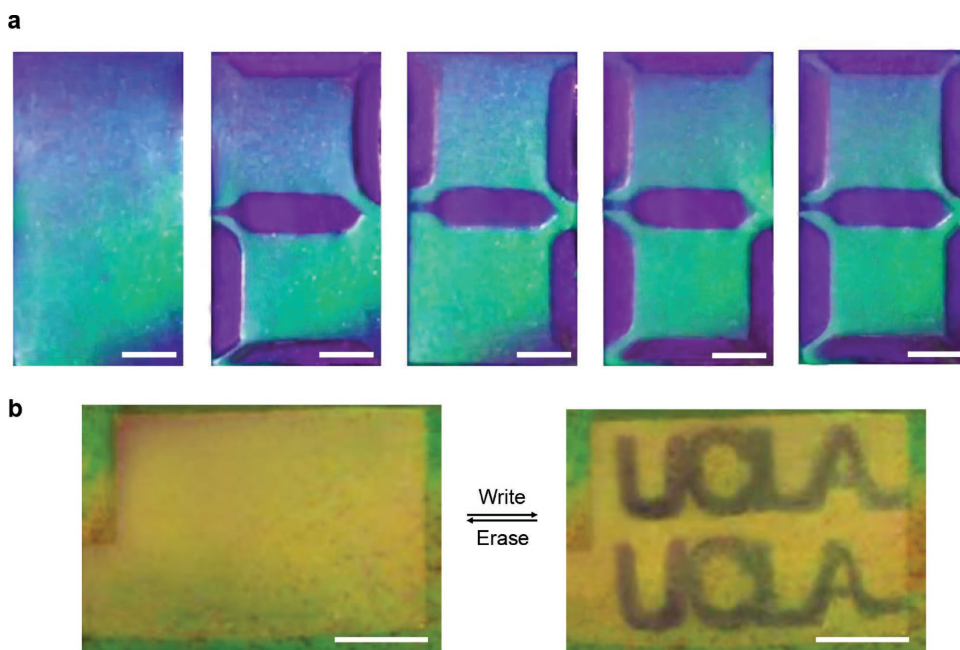
Figure 6. Demonstration of rewritable photonic papers. a) Selected images of a photonic paper sequentially demonstrating digits 0–9. b) Writing and erasing a "UCLA" pattern with font size of 10 on a photonic paper. The scale bars are all 3 mm in length.

electrode defines the resolution of the photonic paper, which for our work was limited by the minimum feature size of the spray coating mask prepared by laser cutter. However, screen printing techniques can create arrays of electrode pixels with feature sizes of ≈50 µm, comparable to current paper printing resolution.[57]

8. Conclusion

We have described a new rewritable photonic nanocomposite derived from $Fe_3O_4@C$ core–shell nanoparticles embedded in a SA-UDA-based bistable electroactive polymer. It is a durable information storage medium that can retain messages indefinitely without energy input, and its high color contrast and high resolution guarantee enduring legibility. It is erased through a simple heating mechanism, which can be adjusted to avoid accidental activation. The nanocomposite is rewritable across several hundred cycles without noticeable degradation. Finally, the electric field writing mechanism opens many practical applications where modern technology can easily control the nanocomposite. In our work, 7-segmented electrodes were designed to display digits; while with electrode pixel arrays, images can be created as desired. Given this material's strengths, it shows promise in replacing information displays with long demonstration times but low refresh frequencies, such as billboards and tags. In future studies, we seek to improve the polymer matrix with the aim of targeting full-color range photonic paper.

9. Experimental Section

Materials: Stearyl acrylate (SA), benzophenone (BP), 2,2-dimethoxy-2-phentlacetophenone (DMPA), and trimethylolpropane trimethacrylate

(TMPTA) were obtained from Sigma-Aldrich. Ferrocene was purchased from Alfa Aesar. Urethane diacrylate (CN9021) was supplied by Startomer. AgNWs with an average diameter of 25–35 µm were provided by Kechuang.

Synthesis of $Fe_3O_4@C$ Core–Shell Nanoparticles: Following the procedure previously reported, with modification:[51,58] In a typical synthesis, ferrocene (0.27 g) was dissolved in acetone (27 mL) through mechanical stirring for 30 min, followed by sonication for another 30 min. Hydrogen peroxide (0.9–1.35 mL) was then added into the mixture dropwise. The amount of hydrogen peroxide determined the size of synthesized nanoparticles. 0.9–1.35 mL was chosen as to synthesize nanoparticles with desired diameters of (110–160 nm). After 30 min of sonication and 1 h of mechanical stirring, the homogenous mixture was transferred to a Teflon-lined stainless steel autoclave (45 mL). The whole setup was left in an oven at 210 °C for 30 h. After synthesis, the product was washed three times with acetone once the autoclave cooled down to room temperature. The final product was left in the ambient environment to dry.

Fabrication of $Fe_3O_4@C$-BSEP Photonic Precursors: The BSEP mixture was prepared by mixing SA and UDA oligomers with 40:60 to 80:20 weight ratios. After adding small amounts of BP and DMPA as cophotoinitiators and TMPTA as the crosslinker, the entire SA-UDA mixture was sonicated for 30 min before use. $Fe_3O_4@C$ powder was added into the SA-UDA mix (4–7 wt%), followed by long sonication to form a uniform photonic precursor.

Preparation of Patterned AgNWs Electrodes: Purchased AgNWs were diluted with methanol and isopropanol in a 1:2:4 weight ratio. The AgNW mixture was shaken by vortex for at least 1 h before use to form a homogeneous electrode film. Specially designed masks were taped onto glass slides before spray coating the AgNWs to make the desired electrode shapes. Scotch Magic Tape was used as the mask material, and it was pre-cut by a laser cutter (Epilog Zing Laser). The AgNW mixture was sprayed coated onto the prepared glass slides with an air gun (Paasche, H0610). After spray coating, the AgNW electrodes were washed once with isopropanol and twice with water.

Fabrication of $Fe_3O_4@C$-BSEP Rewritable Photonic Films with Patterned Electrodes: Two glass slides were precleaned in acetone and spray coated with patterned AgNW-electrodes through pre-cut Scotch Magic Tape

masks. Photonic precursor was then infiltrated in between the two glass slides separated by spacers (90 µm). The infiltrated film was cured under UV light with an external magnet ($\approx$2300 G) for 3 min. After curing, the film was peeled off as a freestanding rewritable photonic film.

Characterization: Reflection spectra were taken using an Ocean Optics USB2000 fiber optic vis–NIR spectrometer with a reflection probe (R600-7) and a tungsten halogen light source (LS-1). TEM images were taken using an FEI T12 Quick CryoEM and CryoET microscope. SEM images were taken by an FEI Nova Nano 230 scanning electron microscope. Magnetization of the Fe_3O_4@C nanoparticles was tested by a MPMS3 Superconducting Quantum Interference Device (SQUID) magnetometer. Shape memory cycle test was conducted with a TA Instrument RSA-G2 Solid Analyzer with a temperature sweep rate of 10 °C min^{-1} and a stretching rate of 0.1 mm s^{-1}. Samples were made to 5 mm in widths and 90 µm in thicknesses. The separation between thin film grips of DMA was set to 4 mm. Other mechanical properties were tested on a TA Instruments RSAIII dynamic mechanical analyzer (DMA). Samples were made to 5 mm in widths and 90 µm thicknesses. The separation between thin film grips of DMA was set to 5 mm. Dynamic temperature sweep tests were operated at a 2 °C min^{-1} ramp rate and 1 Hz frequency. The stress–strain cycles and fracture tests were conducted at 50 °C with a stretching rate of 1 mm s^{-1}. The A high-voltage power supply was built in-house to actuate the Fe_3O_4@C-BSEP nanocomposite films. Resistance measurements for the AgNW electrodes were conducted on a motorized linear stage (Zaber Technologies), measured by a Keithley 2400 digital multimeter, and recorded with a custom LabView code.

Supporting Information

Supporting Information is available from the Wiley Online Library or from the author.

Conflict of Interest

The authors declare no conflict of interest.

[1] Toxics Release Inventory National Analysis, United States Environmental Protection Agency, https://www.epa.gov/sites/production/files/2018-01/documents/tri_national_analysis_2016_complete_0.pdf (accessed: January 2018).

[2] B. K. Ince, Z. Cetecioglu, O. Ince, in *Environmental Management in Practice*, InTech, Rijeka, Croatia **2011**, Ch. 11, pp. 223–246.

[3] B. Comiskey, J. Albert, H. Yoshizawa, J. Jacobson, *Nature* **1998**, *394*, 253.

[4] B.-R. Yang, L. Wang, Y.-C. Wang, J. Qiu, G. Liu, S. Deng, *SID Int. Symp. Dig. Tech. Pap.* **2017**, *48*, 542.

[5] L. Wang, G. S. Liu, Y. C. Wang, J. Su, X. D. Wang, X. Zeng, Z. S. Zhang, S. Z. Deng, H. P. D. Shieh, B. R. Yang, *J. Soc. Inf. Disp.* **2017**, *25*, 384.

[6] M. Wang, Y. Li, H. Du, X. Zhang, H. Gu, R. Ivanov, R. Sprague, Google Patents, *US9423666B2*, **2016**.

[7] X. Wang, H. Zang, P. Li, *SID Symp. Dig. Tech. Pap.* **2006**, *37*, 1587.

[8] P. F. Bai, R. A. Hayes, M. Jin, L. Shui, Z. C. Yi, L. Wang, X. Zhang, G. Zhou, *Prog. Electromagn. Res.* **2014**, *147*, 95.

[9] Y. Deng, B. Tang, A. V. Henzen, G. G. Zhou, *SID Symp. Dig. Tech. Pap.* **2017**, *48*, 535.

[10] Y. K. Fung, D. K. Yang, J. W. Doane, *Proc. SPIE* **1992**, *1664*, 41.

[11] J. W. Doane, D.-K. Yang, L.-C. Chien, Google Patents, *US6104448A*, **2000**.

[12] M. Lightfoot, E. N. Montbach, D. Marhefka, A. A. Khan, Google Patents, *US20180031886A1*, **2018**.

[13] E. N. Montbach, C. I. Braganza, M. Echeverri, D. Marhefka, D. J. Davis, F. Nicholson, A. Khan, *SID Symp. Dig. Tech. Pap.* **2017**, *48*, 1769.

[14] J. Wei, X. Jiao, T. Wang, D. Chen, *ACS Appl. Mater. Interfaces* **2016**, *8*, 29713.

[15] L. Sheng, M. Li, S. Zhu, H. Li, G. Xi, Y. G. Li, Y. Wang, Q. Li, S. Liang, K. Zhong, S. X. Zhang, *Nat. Commun.* **2014**, *5*, 3044.

[16] W. Wang, J. Feng, J. Ye, F. Lyu, Y. S. Liu, J. Guo, Y. Yin, *Nano Lett.* **2017**, *17*, 755.

[17] W. Wang, N. Xie, L. He, Y. Yin, *Nat. Commun.* **2014**, *5*, 5459.

[18] J. Ge, J. Goebl, L. He, Z. Lu, Y. Yin, *Adv. Mater.* **2009**, *21*, 4259.

[19] H. Fudouzi, Y. Xia, *Langmuir* **2003**, *19*, 9653.

[20] P. Jiang, D. W. Smith, J. M. Ballato, S. H. Foulger, *Adv. Mater.* **2005**, *17*, 179.

[21] M. Moirangthem, A. F. Scheers, A. Schenning, *Chem. Commun.* **2018**, *54*, 4425.

[22] H. Wan, X. Li, L. Zhang, X. Li, P. Liu, Z. Jiang, Z. Z. Yu, *ACS Appl. Mater. Interfaces* **2018**, *10*, 5918.

[23] Y. Fang, Y. Ni, S. Y. Leo, B. Wang, V. Basile, C. Taylor, P. Jiang, *ACS Appl. Mater. Interfaces* **2015**, *7*, 23650.

[24] Y. Fang, S. Y. Leo, Y. Ni, J. Wang, B. Wang, L. Yu, Z. Dong, Y. Dai, V. Basile, C. Taylor, P. Jiang, *ACS Appl. Mater. Interfaces* **2017**, *9*, 5457.

[25] S. Y. Leo, W. Zhang, Y. Zhang, Y. Ni, H. Jiang, C. Jones, P. Jiang, V. Basile, C. Taylor, *Small* **2018**, *14*, e1703515.

[26] Y. Fang, Y. Ni, B. Choi, S. Y. Leo, J. Gao, B. Ge, C. Taylor, V. Basile, P. Jiang, *Adv. Mater.* **2015**, *27*, 3696.

[27] Y. Fang, Y. Ni, S. Y. Leo, C. Taylor, V. Basile, P. Jiang, *Nat. Commun.* **2015**, *6*, 7416.

[28] J. Xia, Y. Ying, S. H. Foulger, *Adv. Mater.* **2005**, *17*, 2463.

[29] I. Lee, D. Kim, J. Kal, H. Baek, D. Kwak, D. Go, E. Kim, C. Kang, J. Chung, Y. Jang, *Adv. Mater.* **2010**, *22*, 4973.

[30] K. H. Ko, E. Park, H. Lee, W. Lee, *ACS Appl. Mater. Interfaces* **2018**, *10*, 11776.

[31] T. S. Shim, S. H. Kim, J. Y. Sim, J. M. Lim, S. M. Yang, *Adv. Mater.* **2010**, *22*, 4494.

[32] H. S. Yang, J. Jang, B. S. Lee, T. H. Kang, J. J. Park, W. R. Yu, *Langmuir* **2017**, *33*, 9057.

[33] Z. H. Fang, C. Punckt, E. Y. Leung, H. C. Schniepp, I. A. Aksay, *Appl. Opt.* **2010**, *49*, 6689.

[34] A. C. Arsenault, D. P. Puzzo, I. Manners, G. A. Ozin, *Nat. Photonics* **2007**, *1*, 468.

[35] T. Yin, D. Zhong, J. Liu, X. Liu, H. Yu, S. Qu, *Soft Matter* **2018**, *14*, 1120.

[36] H. Fudouzi, Y. Xia, *Adv. Mater.* **2003**, *15*, 892.

[37] K. Hwang, D. Kwak, C. Kang, D. Kim, Y. Ahn, Y. Kang, *Angew. Chem., Int. Ed. Engl.* **2011**, *50*, 6311.

[38] Y. Lu, C. Meng, H. Xia, G. Zhang, C. Wu, *J. Mater. Chem. C* **2013**, *1*, 6107.

[39] T. J. Park, S. K. Hwang, S. Park, S. H. Cho, T. H. Park, B. Jeong, H. S. Kang, D. Y. Ryu, J. Huh, E. L. Thomas, *ACS Nano* **2015**, *9*, 12158.

[40] H. Kim, J. Ge, J. Kim, S.-E. Choi, H. Lee, H. Lee, W. Park, Y. Yin, S. Kwon, *Nat. Photonics* **2009**, *3*, 534.

[41] I. B. Burgess, L. Mishchenko, B. D. Hatton, M. Kolle, M. Loncar, J. Aizenberg, *J. Am. Chem. Soc.* **2011**, *133*, 12430.

[42] P. K. Kundu, D. Samanta, R. Leizrowice, B. Margulis, H. Zhao, M. Borner, T. Udayabhaskararao, D. Manna, R. Klajn, *Nat. Chem.* **2015**, *7*, 646.

[43] X. Du, T. Li, L. Li, Z. Zhang, T. Wu, *J. Mater. Chem. C* **2015**, *3*, 3542.

[44] M. M. Hawkeye, M. J. Brett, *Adv. Funct. Mater.* **2011**, *21*, 3652.

[45] B. Viel, T. Ruhl, G. P. Hellmann, *Chem. Mater.* **2007**, *19*, 5673.

[46] H. Hu, C. Chen, Q. Chen, *J. Mater. Chem. C* **2013**, *1*, 6013.

[47] H. Li, J. Wang, L. Yang, Y. Song, *Adv. Funct. Mater.* **2008**, *18*, 3258.

[48] Y. Takeoka, M. Watanabe, *Langmuir* **2003**, *19*, 9104.

[49] K. Yoshino, Y. Shimoda, Y. Kawagishi, K. Nakayama, M. Ozaki, *Appl. Phys. Lett.* **1999**, *75*, 932.

[50] A. Seyfoddin, A. Chan, W. T. Chen, I. D. Rupenthal, G. I. Waterhouse, D. Svirskis, *Eur. J. Pharm. Biopharm.* **2015**, *94*, 419.

[51] H. Wang, Y.-B. Sun, Q.-W. Chen, Y.-F. Yu, K. Cheng, *Dalton Trans.* **2010**, *39*, 9565.

[52] J. Ge, Y. Hu, Y. Yin, *Angew. Chem.* **2007**, *119*, 7572.

[53] Z. Ren, W. Hu, C. Liu, S. Li, X. Niu, Q. Pei, *Macromolecules* **2015**, *49*, 134.

[54] L. He, Y. Hu, H. Kim, J. Ge, S. Kwon, Y. Yin, *Nano Lett.* **2010**, *10*, 4708.

[55] C. M. Yakacki, N. S. Satarkar, K. Gall, R. Likos, J. Z. Hilt, *J. Appl. Polym. Sci.* **2009**, *112*, 3166.

[56] R. Pelrine, R. Kornbluh, Q. Pei, J. Joseph, *Science* **2000**, *287*, 836.

[57] J. Liang, K. Tong, Q. Pei, *Adv. Mater.* **2016**, *28*, 5986.

[58] J. Zhang, A. Sun, X. Qiao, C. Chu, C. Wang, T. Chen, J. Guo, G. Xu, *Mater. Res. Express* **2014**, *1*, 045037.